LETTERS
PUBLISHED ONLINE: 22 JUNE 2014 | DOI: 10.1038/NNANO.2014.112
nature nanotechnology

Measurement of collective dynamical mass of Dirac fermions in graphene

Hosang Yoon[1], Carlos Forsythe[2], Lei Wang[3], Nikolaos Tombros[2], Kenji Watanabe[4], Takashi Taniguchi[4], James Hone[3], Philip Kim[2]* and Donhee Ham[1]*

Individual electrons in graphene behave as massless quasiparticles[1–8]. Unexpectedly, it is inferred from plasmonic investigations[9–12] that electrons in graphene must exhibit a non-zero mass when collectively excited. The inertial acceleration of the electron collective mass is essential to explain the behaviour of plasmons in this material, and may be directly measured by accelerating it with a time-varying voltage and quantifying the phase delay of the resulting current. This voltage–current phase relation would manifest as a kinetic inductance, representing the reluctance of the collective mass to accelerate. However, at optical (infrared) frequencies, phase measurements of current are generally difficult, and, at microwave frequencies, the inertial phase delay has been buried under electron scattering[13–15]. Therefore, to date, the collective mass in graphene has defied unequivocal measurement. Here, we directly and precisely measure the kinetic inductance, and therefore the collective mass, by combining device engineering that reduces electron scattering and sensitive microwave phase measurements. Specifically, the encapsulation of graphene between hexagonal boron nitride layers[16], one-dimensional edge contacts[17] and a proximate top gate configured as microwave ground[18,19] together enable the inertial phase delay to be resolved from the electron scattering. Beside its fundamental importance, the kinetic inductance is found to be orders of magnitude larger than the magnetic inductance, which may be utilized to miniaturize radiofrequency integrated circuits. Moreover, its bias dependency heralds a solid-state voltage-controlled inductor to complement the prevalent voltage-controlled capacitor.

The collective excitation of massless fermions in graphene exhibits a non-zero mass. This fact is subsumed under the general theoretical framework of graphene plasmonics[9], yet it can be considered simply. Let electrons in graphene (width W, unit length) be subjected to a voltage difference V across the length. The resulting translation of the Fermi disk in two-dimensional k-space by $\Delta k \ll k_F$ (where k_F is the Fermi wavenumber) from disk A to B (Fig. 1a,b) yields a collective momentum per unit length, $P = n_0 W\hbar\,\Delta k$ (n_0 is the electron density and $\hbar$ the reduced Planck constant). The corresponding collective kinetic energy per unit length (E) is obtained by subtracting the sum of single electron energies $\varepsilon = \hbar v_F k$ (v_F is the Fermi velocity) over disk A from that over disk B. Because E is minimal at $\Delta k = 0$, we must have $E \propto (\Delta k)^2 \propto P^2$ for small Δk (Fig. 1c), from which the collective mass per unit length (M) emerges, satisfying $E = P^2/2M$. Detailed calculation indeed shows $E = W\varepsilon_F/2\pi \times (\Delta k)^2$ (ε_F is the Fermi energy), yielding $M = \pi W n_0^2 \hbar^2/\varepsilon_F$ (Supplementary Section 1).

This emergence of a non-zero collective mass in graphene from its massless individual electrons contrasts sharply with the case of typical conductors, where the non-zero individual electron masses m^* simply sum to the collective mass. Yet, as an analogy to m^*, we can consider an effective collective mass per electron for graphene, $m_c^* \equiv M/(Wn_0) = (\hbar/v_F)\sqrt{(\pi n_0)}$. In fact, this is an insightfully defined theoretical entity called 'plasmon mass' in graphene[10,12,20]. However, the collective mass of graphene electrons, which we set out to measure here, is an observable physical reality that proves the existence of the plasmon mass beyond the theoretical model.

The collective current I associated with the Fermi disk shift (that is, the inertial acceleration of the collective mass M) has an inductive phase relationship with the voltage V causing the acceleration. The associated inductance of kinetic origin can be evaluated by

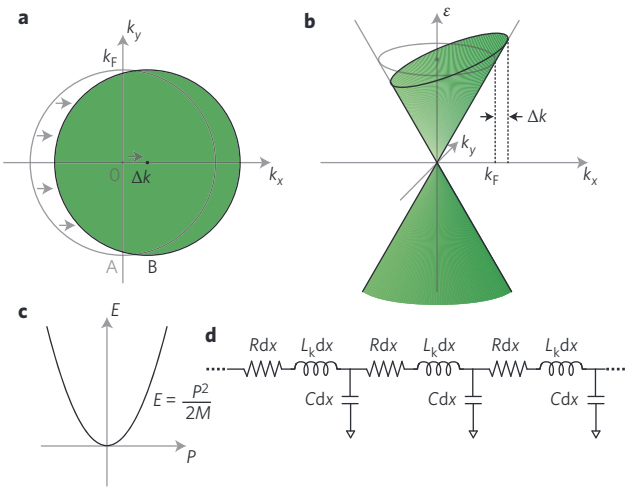

Figure 1 | Collective electrodynamics of graphene electrons. a, Collective motion of graphene electrons subjected to an electric field due to a voltage difference V can be represented as a translation of the Fermi disk in k-space. A (unshaded), at rest; B (shaded), in collective excitation, with an overall shift of Δk (arrows) for the whole Fermi disk. **b**, Alternative representation of the collective electron motion in ε–k space, in conjunction with the massless single electron energy dispersion $\varepsilon = \hbar v_F k$ near the Dirac point. **c**, The collective kinetic energy per unit length, E, exhibits quadratic dependency on the collective momentum per unit length, $P = n_0 W\hbar\Delta k$. The curvature is inversely proportional to the collective dynamical mass per unit length, M. **d**, Graphene as a transmission line. Kinetic inductance L_k, geometric capacitance C and resistance R, all defined per unit length, represent the local collective mass, electrostatic interactions and electron scatterings, respectively. Owing to R, this transmission line is lossy, that is, it does not conserve energy.

[1]School of Engineering and Applied Sciences, Harvard University, 33 Oxford Street, Cambridge, Massachusetts 02138, USA, [2]Department of Physics, Columbia University, New York, New York 10027, USA, [3]Department of Mechanical Engineering, Columbia University, New York, New York 10027, USA, [4]National Institute for Materials Science, Namiki 1-1, Tsukuba, Ibaraki 305-0044, Japan. *e-mail: donhee@seas.harvard.edu; pk2015@columbia.edu

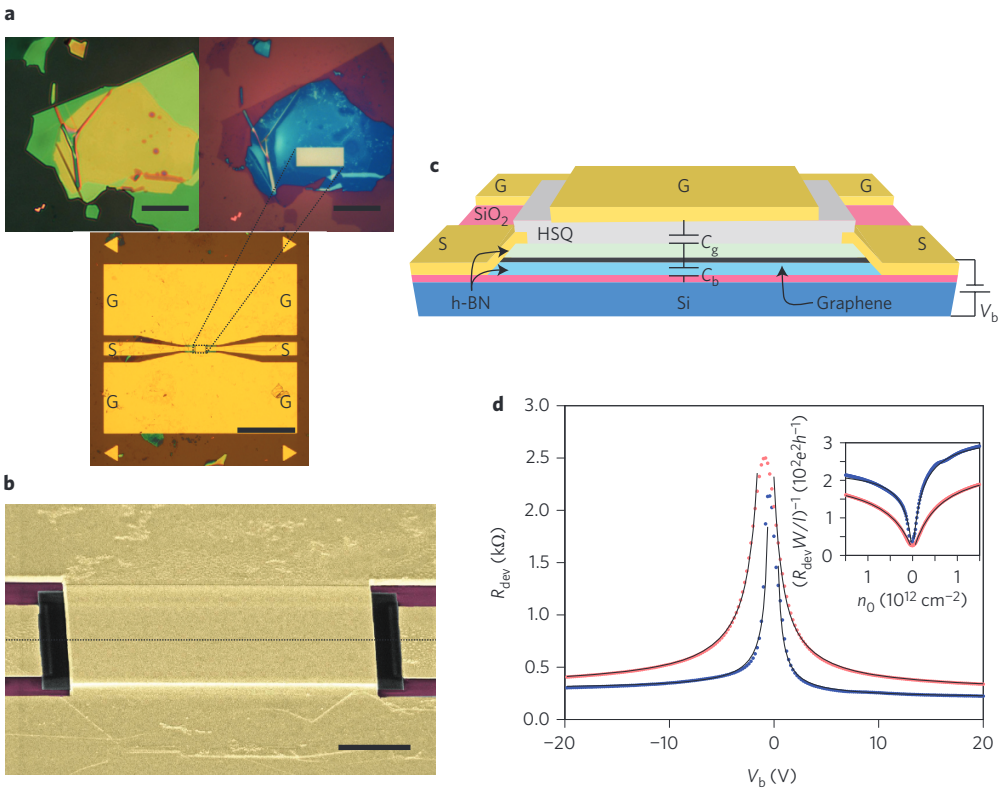

Figure 2 | Device description and d.c. measurements. a, Optical image of the h-BN/graphene/h-BN layered structure before etching (top left, scale bar, 20 μm), after etching (top right, scale bar, 20 μm), and after depositing the CPWs (bottom, scale bar, 100 μm). G, ground; S, signal. **b**, False-colour scanning electron micrograph of the central region of the device that contains the layered structure under the top gate (scale bar, 4 μm). **c**, Schematic diagram of h-BN-encapsulated graphene device with the front face corresponding to the vertical cut through the dotted line in **b**. HSQ, hydrogen silsesquioxane. **d**, Total device resistance R_{dev}, including both in-graphene electron scattering effect R and the contact resistance, measured at 30 K (blue) and 296 K (red) with back-gate bias V_b varied while graphene and the top gate are kept at the same d.c. potential. Inset: Corresponding plot of $(R_{dev}/(l/W))^{-1}$, which is the conductivity that includes the contact effects; $n_0 = C_b/W \times (V_b - V_{b,0})/e$ where $C_b/W = 0.12$ fF μm^{-2} and $V_{b,0} = -0.5$ V (30 K) or $V_{b,0} = -0.9$ V (296 K). Solid curves are fits to $\sigma^{-1} = (n_0 e \mu_C)^{-1} + \rho_s$.

noting $E \propto I^2$, for $I \propto \Delta k$ and $E \propto (\Delta k)^2$; that is, by analogy to magnetic inductance, we can write $E = L_k I^2/2$ with the kinetic inductance per unit length

$$L_k = \frac{\pi\hbar^2}{We^2\varepsilon_F} = \frac{\sqrt{\pi}\hbar}{We^2 v_F} \times \frac{1}{\sqrt{n_0}} \quad (1)$$

(e is elementary charge; Supplementary Section 1). The same underlying physics, namely the quadratic dependence of E on Δk, gives rise to both M and L_k, which are thus intimately related by $M = (e^2 n_0^2 W^2) \times L_k$ (the kinetic inductance represents the 'inertial' reluctance of the collective current to change). Alternatively, we can obtain equation (1) from the Drude model, as we have identified the effective collective mass per electron, m_c^*. Plugging $m_c^* = (\hbar/v_F)\sqrt{(\pi n_0)}$ into the familiar Drude form of kinetic inductance[18,19,21], $L_k = m_c^*/(n_0 e^2 W)$, yields equation (1). This again confirms the deep-seated relation between M and L_k. Note that the graphene kinetic inductance has the peculiar $1/\sqrt{n_0}$ dependence due to graphene's linear single-electron ε–k dispersion (or, equivalently, because m_c^* has the $\sqrt{n_0}$ dependency in the Drude form of kinetic inductance above). This contrasts with the $1/n_0$ dependence of the kinetic inductance of typical conductors, which has long been known from measurements and applied[18,19,21], with quadratic single-electron ε–k dispersion.

To weigh M, we directly measured L_k, essentially by interrogating the voltage–current phase relation in graphene in a microwave transport experiment, with graphene acting as a lossy transmission line[18,19,21–23] (Fig. 1d). This transmission line comprised L_k (which models the local collective mass), the geometric capacitance per unit length C (which models electrostatic interactions) and the resistance per unit length R (which models electron scattering). The magnetic inductance, which is orders of magnitude smaller[18,23] than L_k (Supplementary Section 2), and the quantum capacitance[24], whose effect is far weaker than that of C in our device geometry, were both ignored.

Although the kinetic inductance of graphene can be implied from plasmonic theory[9] and has been theorized explicitly[20,25,26], its direct measurement has been evasive. In far-infrared intensity transmission spectroscopy, the kinetic inductance can be indirectly inferred from the fitting parameter called the 'Drude weight'[10,12,20], but as these experiments do not measure the phase progression of the collective current, they do not unambiguously prove the collective mass and its inertial acceleration. At microwave frequencies, although the voltage–current phase relation can be measured directly, attempts[13–15] to measure L_k have been unsuccessful because R is far larger than the inductive impedance $i\omega L_k$ at microwave frequencies (that is, the kinetic inductor's quality factor[18,23] $Q = \omega L_k/R = \omega\tau$ is far smaller than 1, where τ is the electron scattering time) even in reasonably high-mobility graphene.

In our microwave measurements of L_k, we overcame this difficulty by greatly reducing the electron scattering, and thus R. Specifically, we encapsulated exfoliated graphene between two hexagonal boron nitride (h-BN) layers[16,17] (Fig. 2), significantly reducing the electron scattering originating from disorder. To

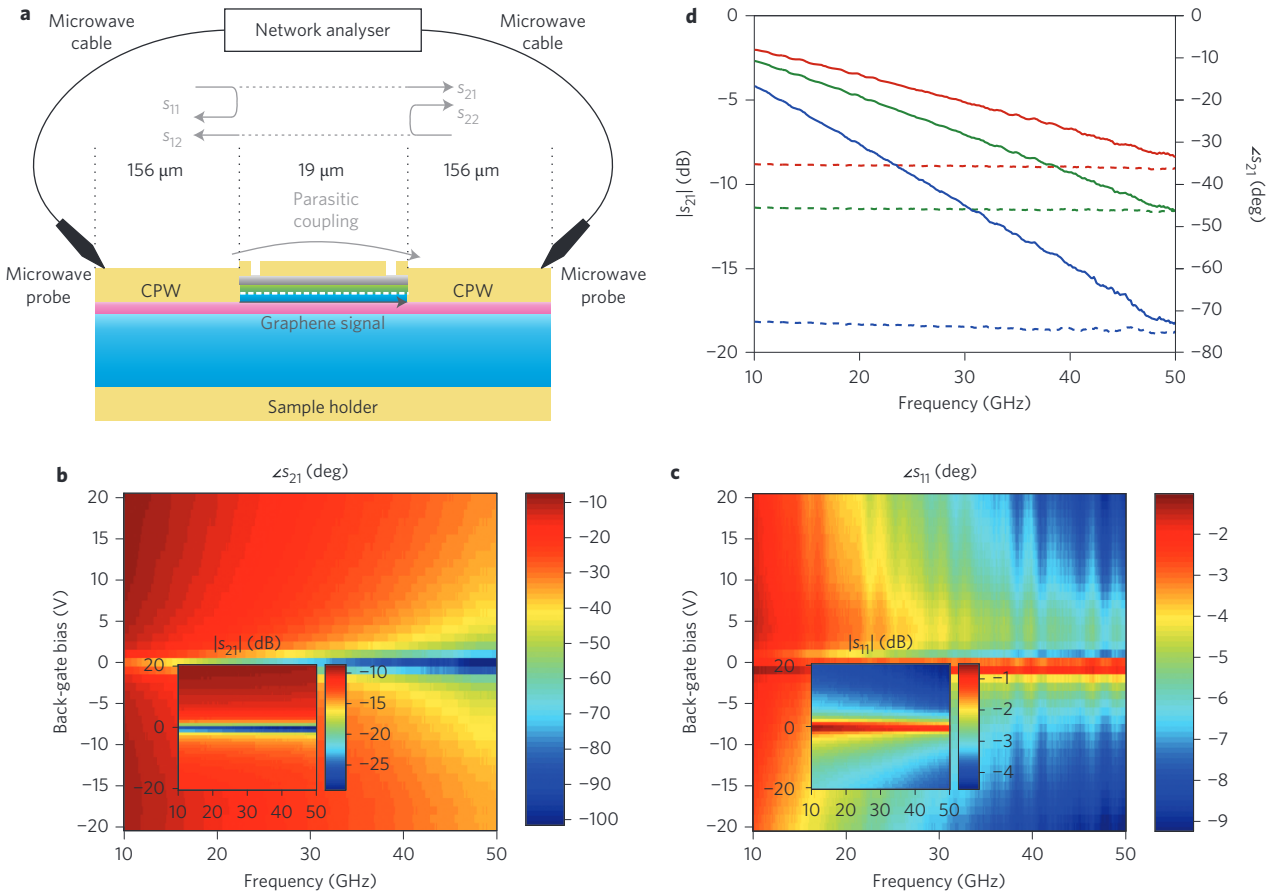

Figure 3 | Microwave *s*-parameter measurements. a, Schematic diagram of the measurement set-up. The *s*-parameters shown are after calibrating out the delay and loss of the cables, probes and on-chip coplanar electromagnetic waveguides (CPWs) and also after de-embedding the parasitic coupling bypassing the graphene. **b**,**c**, Phase (insets, amplitude) of the measured transmission (s_{21}; **b**) and reflection (s_{11}; **c**) parameters after calibration and de-embedding at 30 K. The *s*-parameters with excitation from the opposite side (s_{12} and s_{22}; Supplementary Section 3.1) look almost identical to s_{21} and s_{11}. **d**, Selected data from **b**, specifically, transmission phase ($\angle s_{21}$; solid curves) and amplitude ($|s_{21}|$; dashed curves) at three representative bias values $V_b = 1$ V (blue), 4 V (green) and 20 V (red).

reduce electron–phonon scattering, the device was cooled to 30 K. Furthermore, to reduce additional electron scattering in the contact regions at both ends of the graphene, we made one-dimensional, edge-only contacts to the graphene by etching the stack of h-BN and graphene into a desired shape ($W = 7.5$ μm; length $l = 19.0$ μm) and depositing metal onto the side edges[17] (Fig. 2a–c). Graphene was connected to the signal (S) lines of on-chip coplanar electromagnetic waveguides (CPWs) to the left and right via the abovementioned edge-only contacts, and was placed under a top gate merged with the ground (G) lines of the CPWs.

To first confirm the scattering reduction, we measured the d.c. resistance between the S lines using a lock-in technique, with the graphene and top gate kept at the same d.c. potential. The total device resistance R_{dev}, which includes the effects of both R and contact resistances, was measured as a function of the back-gate potential V_b that sets the carrier density n_0 (Fig. 2d). At 30 K, it shows charge neutrality at $V_{b,0} = -0.5$ V and excellent performance in the electron-doped region ($V_b > V_{b,0}$), which is fit well by the widely adopted conductivity formula[16,27] $\sigma^{-1} = (n_0 e \mu_C)^{-1} + \rho_s$, with $\mu_C = 390{,}000\ cm^2\ V^{-1}\ s^{-1}$ representing the n_0-independent mobility due to long-range scattering and $\rho_s = 80\ \Omega$ representing short-range scattering. At room temperature, μ_C is $110{,}000\ cm^2\ V^{-1}\ s^{-1}$ in the electron-doped region. This high μ_C even at room temperature confirms the decisive reduction in R due to the h-BN encapsulation[16,17], and the approximately fourfold larger μ_C at 30 K shows a further reduction in R due to decreased scattering with phonons. See Methods for a detailed analysis.

To measure L_k with the reduced R, we used a vector network analyser to launch microwaves (10–50 GHz) onto the CPWs and recorded the amplitude and phase response of their transmission (s_{21}, s_{12}) and reflection (s_{11}, s_{22}) (Fig. 3a). The network analyser was connected to the graphene via cables, probes and the CPWs, whose phase delay and loss were calibrated out. The direct parasitic coupling between the left and right CPWs/probes bypassing the graphene channel was separately measured and de-embedded[23]. L_k was then extracted from the resulting *s*-parameters.

Were it not for the R reduction, the L_k extraction would be daunting, as can be seen from the expression for the phase delay per unit length (ϕ) through the graphene transmission line (Fig. 1d), $\phi \approx (\omega RC/2)^{1/2} + (\omega^3/8)^{1/2}(C/R)^{1/2} \times L_k \equiv \phi_1 + \phi_2$ (Supplementary Section 4). As only the second term, ϕ_2, contains L_k, ϕ_2 should be large enough to enable L_k extraction. With large R (or $Q = \omega L_k/R \ll 1$), ϕ_2 would be masked by ϕ_1 as $\phi_2/\phi_1 = Q/2$, and $\phi_2 \propto 1/\sqrt{R}$ itself would be miniscule. Our R reduction is thus critical for L_k extraction. This alone, albeit crucial, is still insufficient for L_k extraction, as the improved Q is still smaller than 1. Another critical step is to enhance C; although this does not alter ϕ_2/ϕ_1, it further increases $\phi_2 (\propto \sqrt{C})$ itself. We enhance C via the proximate top gate, which, merged with the CPWs' G lines (Fig. 2a–c), serves as a well-defined microwave ground[18,19]; hence, for microwave signalling, $C = C_g$, the capacitance between graphene and the grounded top

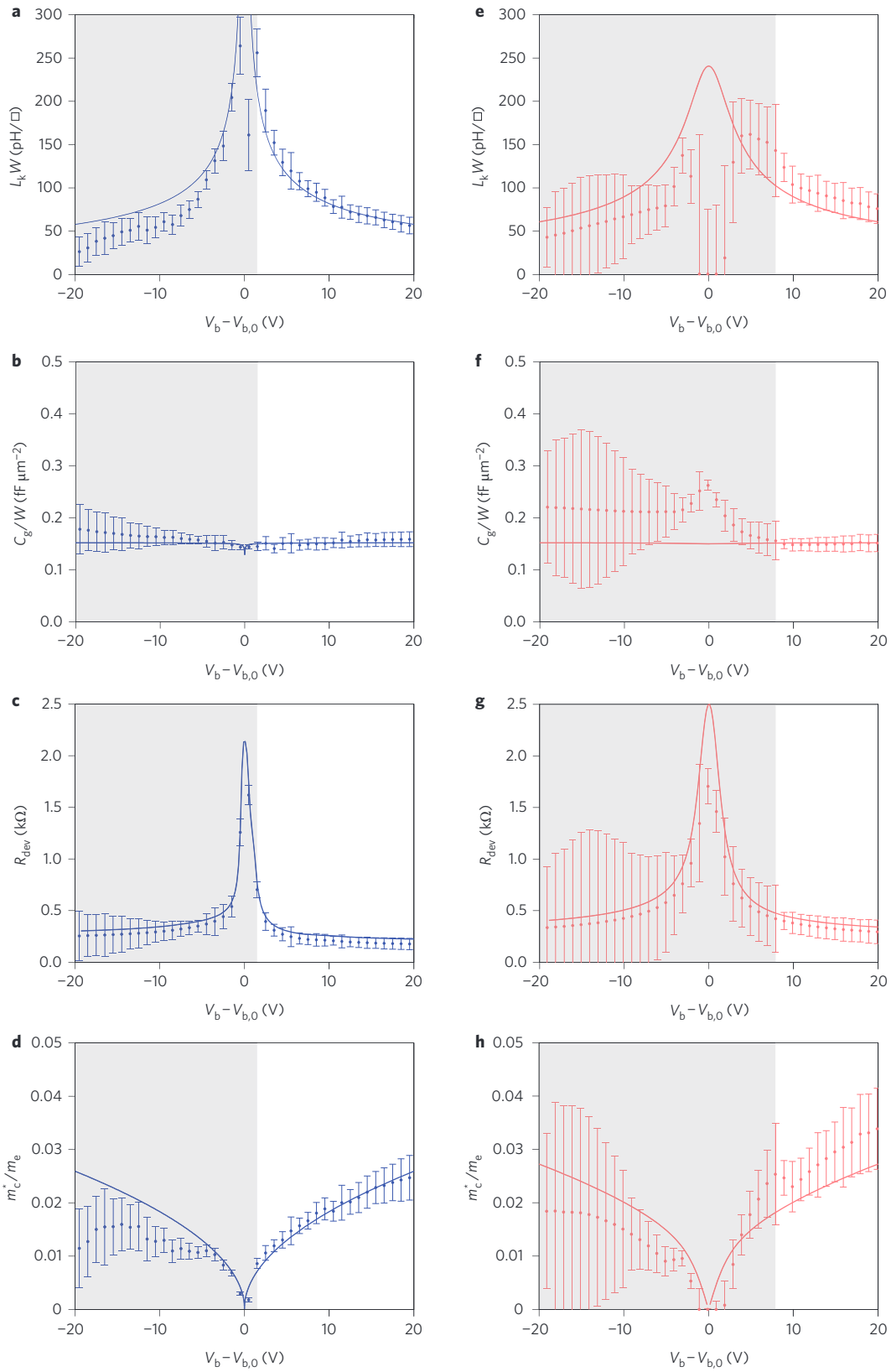

Figure 4 | Extracted graphene kinetic inductance and collective electron mass. a–h, Kinetic inductance per square L_kW (**a**,**e**), graphene to top-gate capacitance per unit area C_g/W (**b**,**f**), total device resistance R_{dev} (**c**,**g**), and collective dynamical mass per electron, or plasmon mass m_c^* (**d**,**h**), extracted from the measured *s*-parameters for various V_b at 30 K (blue; **a–d**) and 296 K (red; **e–h**), respectively. Error bars indicate standard errors of the extracted parameters (Supplementary Section 6.1). The solid curves in L_kW, C_g/W and m_c^* plots represent theoretical predictions. The small dip in capacitance at charge neutrality is due to the otherwise negligible effect of quantum capacitance in our device geometry. The solid curves in R_{dev} plots are those measured under d.c. conditions, that is, they are re-displayed from Fig. 2d. Shaded areas indicate bias regions where extraction was less reliable (see text).

gate, and we estimate $C/W = C_g/W \approx 0.15$ fF μm^{-2} (Fig. 2c). See Methods for the full rationale.

Figure 3b,c presents colour maps of the phase and amplitude of the transmission (s_{21}; Fig. 3b) and reflection (s_{11}; Fig. 3c) parameters measured at 30 K as functions of V_b (thus n_0) and frequency. The s_{21} and s_{11} amplitudes exhibit a sharp drop and peak, respectively, near the charge neutrality point $V_{b,0} = -0.5$ V, because n_0 is greatly reduced. Figure 3d shows s_{21} at three selected V_b values in the electron-doped region to show that our device *s*-parameters are amenable to L_k extraction. Were it not for the *R* reduction and *C* enhancement, the measured s_{21} phase and its portion contributed by L_k, which are intimately related to ϕ and ϕ_2, respectively, would exhibit far smaller absolute values as well as far smaller differences with the variation in V_b (and thus with the corresponding variation of L_k), hampering L_k extraction (Supplementary Section 5).

To determine L_k from the measured *s*-parameters for each bias, we used the microwave optimization method[18]. We added contact models to both sides of the transmission line model (Fig. 1d with $C = C_g$) and altered the component values (L_k, C_g, *R* and contact resistances) until the *s*-parameters (s_{11}, s_{21}, s_{12}, s_{22}) calculated from the model best fit the measured *s*-parameters across the frequency range in the least-squares method (Supplementary Section 6). In this way, we determined L_k and other component values at each V_b. The reliability of this method is based on the model's reflection of physics and the fact that the limited number of model components must reproduce the vastly larger number of measured *s*-parameters over the frequency range. Its cogency will be confirmed ultimately by the consistency of the extracted values and other measured parameters, and with the physical theory. The same experiment repeated on a completely different device led to almost identical results (Supplementary Section 3.2), further attesting to the reliability of this approach.

Figure 4 displays L_k, C_g and *R* as determined for each V_b at 30 K (Fig. 4a–c) and 296 K (Fig. 4e–g). We first focus on the 30 K results in the electron-doped region ($V_b > V_{b,0}$) that showed the best d.c. characteristics (Fig. 2d), in particular in the region away from $V_{b,0}$ (unshaded regions in Fig. 4a–c). As expected, the extracted C_g/W stays nearly constant (Fig. 4b), with negligible variation due to the quantum capacitance effect[24], and its value of ~0.15 fF μm^{-2} is consistent with the value estimated earlier. Also, the extracted L_k (Fig. 4a) closely follows the theoretical curve given by equation (1) with $v_F = 10^6$ m s^{-1}, demonstrating, for the first time, an accurate direct measurement of the kinetic inductance in graphene. The small deviation of the observed L_k from the theoretical curve in this unshaded region of the electron-doped regime, becoming more pronounced toward $V_{b,0}$, is attributed predominantly to imperfect calibration and parasitic-signal de-embedding. In principle, the deviation may also have contributions from the weak variations of v_F due to dielectric screening[28], impurities[28] and electron–electron interaction effects[20,29], but the dominant effect of imperfect calibration and parasitic-signal de-embedding obviates the separate study of these effects. Further confirming the consistency of the technique, R_{dev} extracted from the *s*-parameters agrees well with R_{dev} measured under d.c. conditions (Fig. 4c). Finally, from the measured L_k, we obtain the collective mass $M = (e^2 n_0^2 W^2) \times L_k$ and then the collective mass per electron discussed earlier, $m_c^* = M/(Wn_0) = (e^2 n_0 W) \times L_k$. It closely follows the theory (Fig. 4d): m_c^* is a few percent of the intrinsic electron mass $m_e = 9.1 \times 10^{-31}$ kg and distinctively shows the graphene-specific $\sqrt{n_0}$ dependence.

The 296 K data in the unshaded regions in Fig. 4e–h show similar results, but with pronounced errors. This is due to the approximately fourfold increase in *R* at 296 K, highlighting the challenge in measurements of reactance from sub-unit *Q* devices where even a moderate *Q* degradation can drastically affect measurement results. Although not as accurate as the 30 K data, the 296 K data still present a firm direct proof of L_k and collective dynamical mass that earlier works have failed to observe[13–15], enabled by the h-BN graphene interface and proximate gating. Additionally, the 296 K data serve to attest to the cogency of the 30 K data once again, as their juxtaposition highlights the smaller deviations and standard errors in the 30 K data.

Near charge neutrality and in the hole-doped region ($V_b < V_{b,0}$) (shaded regions, Fig. 4), the extracted L_k at 30 K or 296 K exhibits a more appreciable deviation from theory. Near neutrality, as the transmission amplitude is significantly smaller due to the sharply reduced n_0 (Fig. 3b), the raw transmission *s*-parameters (before removal of the graphene-bypassing parasitic signal) are dominated by the parasitic signal itself, resulting in highly distorted parasitic-signal de-embedded *s*-parameters. As our model neglects the distortion effect, even the best-optimized model *s*-parameters poorly fit the distorted *s*-parameters, therefore causing the discrepancy. The hole-doped regime discrepancy is also caused by the distorted *s*-parameters, which, this time, arise from the asymmetric behaviour of the contacts caused by a workfunction mismatch[17]. This non-ideal behaviour of the metal contact with the hole-doped graphene is not captured by our model (Supplementary Section 6.2).

Beside its fundamental importance for graphene electrodynamics and plasmonics, our work may offer exciting new technological opportunities. The graphene kinetic inductance is orders of magnitude larger than the magnetic inductance at similar dimensions, and so could be used in the future to substantially miniaturize inductors, as it allows one to obtain the same inductance value in orders-of-magnitude smaller areas (Supplementary Section 2). Radiofrequency integrated circuits, prevalent in communication and computing systems, are disadvantaged by the large areas that magnetic inductors occupy. Accordingly, these high-frequency applications may benefit greatly from harnessing the graphene kinetic inductance. Better room-temperature scalability and facile tunability compared with traditional kinetic inductors of superconductors and semiconductor two-dimensional gases also bode well in this regard, as the graphene mobility continues to improve. Furthermore, the bias dependency renders graphene a natural voltage-controlled tunable kinetic inductor as a counterpart to the prevalent voltage-controlled semiconductor capacitor.

Methods

Fabrication and measurements. We fabricated h-BN encapsulated graphene by mechanical exfoliation and polymer-free mechanical transfer of h-BN single crystals and graphene through optical alignment[17]. High resistivity (>5,000 Ω cm) silicon wafers coated with 285-nm-thick thermal oxide were used as the substrate to minimize high-frequency substrate losses. Optical differentiation and Raman spectroscopy were used to confirm that the graphene was single-layered. Contacts[17] and waveguides were created by thermal evaporation of Cr/Pd/Au (1/10/300 nm), with dimensions defined by electron beam lithography and inductively coupled plasma etching.

Measurements took place in a Lake Shore Cryotronics cryogenic probe station at feedback-controlled temperatures in the dark. The d.c. resistance measurements were performed using a Stanford Research Systems SR830 lock-in amplifier and a DL Instruments 1211 current preamplifier. Microwave *s*-parameter measurements were performed using an Agilent E8364A vector network analyser, and the calibration was performed using a NIST-style multiline TRL technique[30] at each temperature just before the measurement. The parasitic coupling bypassing the graphene device was measured on a separate device with identical CPW structures but with no h-BN encapsulated graphene, and was then de-embedded from the measured *s*-parameters of the main device[23]. The design of the CPWs was carried out using a Sonnet frequency-domain electromagnetic field solver. The CPW dimensions were chosen to match the 50 Ω characteristic impedance of the network analyser, cables and probes[23].

Further analysis of d.c. resistance measurements. The inset to Fig. 2d plots $\sigma \equiv (R_{dev}/(l/W))^{-1}$, which was fit to $\sigma^{-1} = (n_0 e \mu_C)^{-1} + \rho_s$ via the least-squares method. The resulting μ_C is only a lower bound of the actual graphene mobility, because the conductivity in this two-probe measurement inevitably includes the contact effects. The electron-doped region ($V_b > V_{b,0}$) showed $\mu_C =$ 390,000 cm^2 V^{-1} s^{-1} and $\rho_s = 80$ Ω at 30 K, but the hole-doped region ($V_b < V_{b,0}$) showed slightly lower $\mu_C = 320{,}000$ cm^2 V^{-1} s^{-1} and higher $\rho_s = 110$ Ω at 30 K due to the contact characteristics[17].

Device design implications from ϕ. The equation $\phi \approx (\omega RC/2)^{1/2} + (\omega^3/8)^{1/2}(C/R)^{1/2} \times L_k \equiv \phi_1 + \phi_2$ provides a guideline to design a device suitable for extracting L_k. Note that only the second term, ϕ_2, contains the effect of L_k. With large R or with $Q = \omega L_k/R \ll 1$, extraction of L_k is challenging because $\phi_2 = (Q/2)\phi_1$ is entirely swamped by ϕ_1 and $\phi_2 \propto 1/\sqrt{R}$ itself may fall below the phase measurement uncertainty ϕ_e (this phase measurement uncertainty originates from the limitations of the network analyser, imperfect calibration, and non-ideal parasitic signal de-embedding). This is why we first reduced R via the h-BN encapsulation of graphene and 30 K operation, which amplifies ϕ_2 and attenuates ϕ_1 with improved $Q = 2\phi_2/\phi_1$. This crucial step alone, however, is insufficient, as the improved Q (~0.2–0.8) is still smaller than 1. Thus, our second enabling step is to enhance C using the proximate top gating. Although this does not change $Q = 2\phi_2/\phi_1$, it further increases $\phi_2 \propto \sqrt{C}$ to ensure $\phi_2 > \phi_e$. In fact, the increased C also reduces ϕ_e, by lowering the characteristic impedance of the graphene channel toward 50 Ω (Supplementary Section 4), thus allowing a better impedance match of the graphene device to the measurement environment and in turn reducing the parasitic signal and its contribution to ϕ_e. Importantly, the R reduction and C enhancement above also make ϕ_2 more sensitive to L_k variation, as seen from the factor $(C/R)^{1/2}$ in ϕ_2, thereby increasing the accuracy of L_k extraction.

Estimation of C. To estimate the enhanced value of C, we first note that only the capacitance C_g between the graphene and the proximate top gate contributes to C, that is, $C = C_g$, because the top gate merged with the CPW G lines (Fig. 2a–c) serves as a well-defined microwave ground[18,19]. In contrast, the silicon back gate, untapped to the G lines, 'floats' in microwave signalling, largely because its connection to the d.c. bias line exhibits a very large inductive impedance and also because the silicon has a high resistivity. Therefore, the capacitance C_b between the graphene and the back gate is irrelevant for microwave signalling. As 44-nm-thick top h-BN ($\kappa \approx 7$)[28,31] and ~150-nm-thick hydrogen silsesquioxane (HSQ; $\kappa \approx 2.8$–3.0)[32] lie between the graphene and the grounded proximate top gate, C_g/W is estimated to be 0.15 fF μm^{-2}, which is far larger than the capacitance of ungated graphene[22].

Received 26 December 2013; accepted 9 May 2014; published online 22 June 2014

References

1. Novoselov, K. S. *et al.* Two-dimensional gas of massless Dirac fermions in graphene. *Nature* **438,** 197–200 (2005).
2. Zhang, Y., Tan, Y-W., Stormer, H. L. & Kim, P. Experimental observation of the quantum Hall effect and Berry's phase in graphene. *Nature* **438,** 201–204 (2005).
3. Geim, A. K. & Novoselov, K. S. The rise of graphene. *Nature Mater.* **6,** 183–191 (2007).
4. Castro Neto, A. H., Guinea, F., Peres, N. M. R., Novoselov, K. S. & Geim, A. K. The electronic properties of graphene. *Rev. Mod. Phys.* **81,** 109–162 (2009).
5. Das Sarma, S., Adam, S., Hwang, E. H. & Rossi, E. Electronic transport in two-dimensional graphene. *Rev. Mod. Phys.* **83,** 407–470 (2011).
6. Koppens, F. H. L., Chang, D. E. & García de Abajo, F. J. Graphene plasmonics: a platform for strong light–matter interactions. *Nano Lett.* **11,** 3370–3377 (2011).
7. Chen, J. *et al.* Optical nano-imaging of gate-tunable graphene plasmons. *Nature* **487,** 77–81 (2012).
8. Yeung, K. Y. M. *et al.* Far-infrared graphene plasmonic crystals for plasmonic band engineering. *Nano Lett.* **14,** 2479–2484 (2014).
9. Hwang, E. H. & Das Sarma, S. Dielectric function, screening, and plasmons in two-dimensional graphene. *Phys. Rev. B* **75,** 205418 (2007).
10. Grigorenko, A. N., Polini, M. & Novoselov, K. S. Graphene plasmonics. *Nature Photon.* **6,** 749–758 (2012).
11. Ju, L. *et al.* Graphene plasmonics for tunable terahertz metamaterials. *Nature Nanotech.* **6,** 630–634 (2011).
12. Yan, H. *et al.* Tunable infrared plasmonic devices using graphene/insulator stacks. *Nature Nanotech.* **7,** 330–334 (2012).
13. Deligeorgis, G. *et al.* Microwave propagation in graphene. *Appl. Phys. Lett.* **95,** 073107 (2009).
14. Lee, H-J., Kim, E., Yook, J-G. & Jung, J. Intrinsic characteristics of transmission line of graphenes at microwave frequencies. *Appl. Phys. Lett.* **100,** 223102 (2012).
15. Jeon, D-Y. *et al.* Radio-frequency electrical characteristics of single layer graphene. *Jpn. J. Appl. Phys.* **48,** 091601 (2009).
16. Dean, C. R. *et al.* Boron nitride substrates for high-quality graphene electronics. *Nature Nanotech.* **5,** 722–726 (2010).
17. Wang, L. *et al.* One-dimensional electrical contact to a two-dimensional material. *Science* **342,** 614–617 (2013).
18. Andress, W. F. *et al.* Ultra-subwavelength two-dimensional plasmonic circuits. *Nano Lett.* **12,** 2272–2277 (2012).
19. Yeung, K. Y. M. *et al.* Two-path solid-state interferometry using ultra-subwavelength two-dimensional plasmonic waves. *Appl. Phys. Lett.* **102,** 021104 (2013).
20. Abedinpour, S. H. *et al.* Drude weight, plasmon dispersion, and ac conductivity in doped graphene sheets. *Phys. Rev. B* **84,** 045429 (2011).
21. Burke, P. J., Spielman, I. B., Eisenstein, J. P., Pfeiffer, L. N. & West, K. W. High frequency conductivity of the high-mobility two-dimensional electron gas. *Appl. Phys. Lett.* **76,** 745–747 (2000).
22. Rana, F. Graphene terahertz plasmon oscillators. *IEEE Trans. Nanotechnol.* **7,** 91–99 (2008).
23. Yoon, H., Yeung, K. Y. M., Umansky, V. & Ham, D. A Newtonian approach to extraordinarily strong negative refraction. *Nature* **488,** 65–69 (2012).
24. Xia, J., Chen, F., Li, J. & Tao, N. Measurement of the quantum capacitance of graphene. *Nature Nanotech.* **4,** 505–509 (2009).
25. Chauhan, J. & Guo, J. Assessment of high-frequency performance limits of graphene field-effect transistors. *Nano Res.* **4,** 571–579 (2011).
26. Yoon, H., Yeung, K. Y. M., Kim, P. & Ham, D. Plasmonics with two-dimensional conductors. *Phil. Trans. R. Soc. Lond. A* **372,** 20130104 (2014).
27. Jang, C. *et al.* Tuning the effective fine structure constant in graphene: opposing effects of dielectric screening on short- and long-range potential scattering. *Phys. Rev. Lett.* **101,** 146805 (2008).
28. Hwang, C. *et al.* Fermi velocity engineering in graphene by substrate modification. *Sci. Rep.* **2,** 590 (2012).
29. Elias, D. C. *et al.* Dirac cones reshaped by interaction effects in suspended graphene. *Nature Phys.* **7,** 701–704 (2011).
30. Marks, R. B. A multiline method of network analyzer calibration. *IEEE Trans. Microw. Theory Tech.* **39,** 1205–1215 (1991).
31. Ohba, N., Miwa, K., Nagasako, N. & Fukumoto, A. First-principles study on structural, dielectric, and dynamical properties for three BN polytypes. *Phys. Rev. B* **63,** 115207 (2001).
32. Maex, K. *et al.* Low dielectric constant materials for microelectronics. *J. Appl. Phys.* **93,** 8793–8841 (2003).

Acknowledgements

D.H. and H.Y. acknowledge support from the Air Force Office of Scientific Research (contract no. FA9550-13-1-0211), from the Office of Naval Research (contract no. N00014-13-1-0806), from the National Science Foundation (NSF; contract no. DMR-1231319), from the Samsung Advanced Institute of Technology and its Global Research Opportunity programme (contract no. A18960). P.K. acknowledges support from the Nano Material Technology Development Program through the National Research Foundation of Korea (NRF) funded by the Ministry of Science, ICT and Future Planning (2012M3A7B4049966). J.H. and L.W. acknowledge support from the NSF (contract no. DMR-1124894) and the Office of Naval Research (award no. N000141310662). C.F. acknowledges support of the Columbia Optics and Quantum Electronics IGERT under NSF grant DGE-1069420. N.T. acknowledges support from the Netherlands Organisation for Scientific Research Device fabrication was performed in part at the Center for Nanoscale Systems at Harvard University.

Author contributions

H.Y., P.K. and D.H. conceived the project. K.W. and T.T. fabricated the h-BN. H.Y., C.F., L.W., N.T. and J.H. fabricated the stacked layers of h-BN, graphene and h-BN. H.Y. designed the device. H.Y. and C.F. fabricated the device. H.Y. performed the experiments. H.Y., P.K. and D.H. analysed the data. H.Y., P.K. and D.H. wrote the paper. All authors discussed the results and reviewed the manuscript.

Additional information

Supplementary information is available in the online version of the paper. Reprints and permissions information is available online at www.nature.com/reprints. Correspondence and requests for materials should be addressed to P.K. and D.H.

Competing financial interests

The authors declare no competing financial interests.